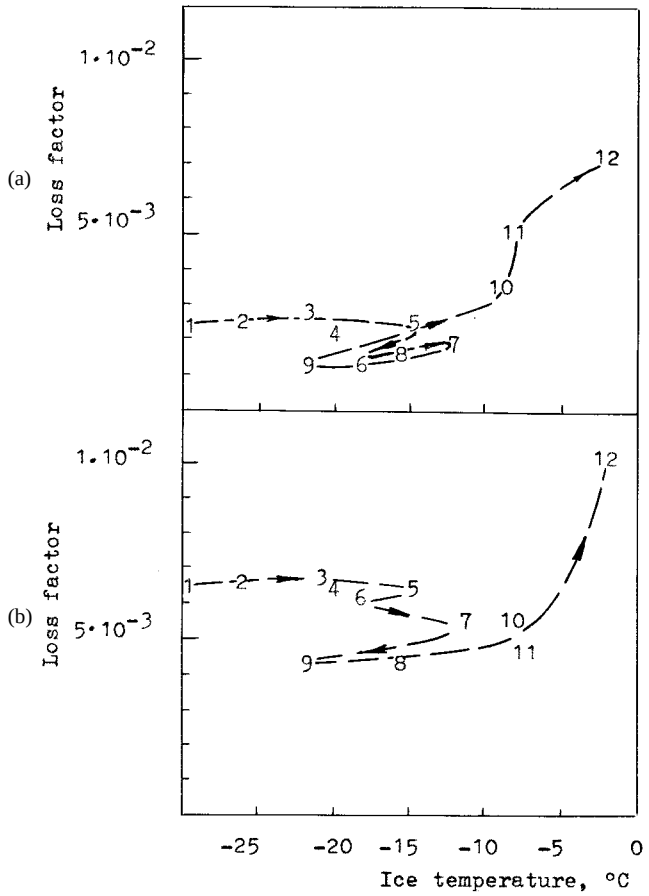

Fig. 3. (a) Observation of ε'' change of ice slab on duraluminum mold at 13.5 GHz. Points (1–3) correspond to the ice time existence in one day; (4) two days; (5) 32 days; (9–10) 47 days; (11) 66 days; and (12) 85 days. (b) The measurements analogous to (a) at 37.5 GHz.

the other hand, quick freezing may produce a specific distribution of salt concentration in ice volume.

However, the main result of the measurements, as it follows from Figs. 2 and 3, is the hysteresis of ε'' in the case of slow-cycle temperature change for many days. Our other experiments with different temperature conditions and with long-time measurements also indicated the effect of ambiguity of electromagnetic losses.

The discussion on hysteresis of the real part of ice dielectric permittivity at 1 kHz was published earlier in [7]. It was observed for the ice that formed the 2% NaCl solution. This experiment lasted for about an hour. However, this observation was interpreted as the influence of the heat of phase transition. In our experiments, the analogous explanation is not true because there was a small amount of salt and a long period of keeping ice at a low-ambient temperature.

We conclude that the hysteresis effect in our experiments may be connected with the existence of supercooling salt microscopic inclusions at temperatures lower than eutectic point, where they are in a liquid state. The possible supercooling temperature is determined by the shape and the size of liquid inclusions. It seems that their metamorphism determine the volume-liquid concentration and, consequently, the imaginary part of dielectric permittivity. The determination of the exact origin of electromagnetic-loss ambiguity requires a more detailed investigation of freshwater ice structure and physical and chemical peculiarities of inclusions.

V. Conclusions

There are significant time changes of the imaginary part of dielectric permittivity even for constant-value salt-impurity concentration in freshwater ice. Different values of electromagnetic loss were experimentally observed at the identical temperature. Thus, for the determination of ice dielectric loss, we must take into account the ice-time existence after water is frozen, the ice-temperature history, and the inclusions characteristics. Disregarding these conditions in previous papers led not so much to measurement errors, but to the description of ice with different structures. Therefore, the cryosphere remote sensing requires taking into account the time changeability of ice electromagnetic properties.

References

[1] A. Stogryn, "A study of the microwave brightness temperature of snow from the point of strong fluctuation theory," *IEEE Trans. Geosci. Remote Sensing*, vol. GE-24, pp. 220–231, Mar. 1986.
[2] S. C. Warren, "Optical constants of ice from the ultraviolet to the microwave," *Appl. Opt.*, vol. 23, no. 8, pp. 1206–1225, 1984.
[3] C. Matzler and U. Wegmuller, "Dielectric properties of freshwater ice at microwave frequencies," *J. Phys. D, Appl. Phys.*, vol. 20, pp. 1623–1630, 1987; Errata in *J. Phys. D, Appl. Phys.*, vol. 21, p. 1660, 1988.
[4] L. Levi and L. Lubart, "On the electric properties of ice doped with NH_4F," *Phys. Kondens. Materie*, vol. 7, pp. 368–371, 1968.
[5] I. G. Young and R. E. Salomon, "Dielectric behavior of ice with HCl impurity," *J. Chem. Phys.*, vol. 48, no. 4, pp. 1635–1644, 1968.
[6] G. S. Bordonski and S. D. Krylov, "Radio brightness variation of freshwater ice cover in winter period," *Izvestya Academii Nauk Rossii Seria Fiziki Atmosfery i Okeana*, vol. 29, no. 6, pp. 842–847, 1993.
[7] V. V. Bogorodsky and G. P. Hohlov, "Influence of some salt components and its composition on ice electrical properties," *Proc. Arct. Antarct. Inst.*, in Russian, vol. 295, pp. 89–95, 1970.

Radiometric Sensitivity Computation in Aperture Synthesis Interferometric Radiometry

Adriano Camps, Ignasi Corbella, Javier Bará, and Francesc Torres

***Abstract*— This paper is concerned with the radiometric sensitivity computation of an aperture synthesis interferometric radiometer devoted to earth observation. The impact of system parameters and the use of simultaneous redundant measurements are analyzed. The Interferometric Radiometer Uncertainty Principle is presented; it quantifies the relationship between radiometric sensitivity and angular resolution.**

***Index Terms*—Interferometry, radiometry, remote sensing, sensitivity.**

I. Introduction

An interferometric radiometer measures the correlation between the analytic signals collected by different antennas [$S_1(t)$ and $S_2(t)$]. These correlations provide the samples of the so-called visibility

Manuscript received December 27, 1995; revised July 2, 1997. This work was supported by the European Space Agency. within the framework of ESA MIRAS CCN 2, Work Order 10, ESTEC Contract 9777/92/NL/PB activities, with MATRA MARCONI SPACE as main contractor.

The authors are with the Department of Signal Theory and Communications, Universitat Politècnica de Catalunya, 08034 Barcelona, Spain (e-mail: camps@voltor.upc.es).

Publisher Item Identifier S 0196-2892(98)00737-2.

function, which has dimensions of Kelvin.

$$V_{1,2}(u,v) = \tfrac{1}{2}E[S_1(t)S_2^*(t)] = \iint_{\xi^2+\eta^2\le 1} T(\xi,\eta)\tilde{r}_{12}\left(-\frac{u\xi+v\eta}{c}\right) \cdot e^{-j2\pi(u\xi+v\eta)}\,d\xi\,d\eta \quad (1)$$

where (u, v) is the baseline and is equal to the difference between the antenna positions over the XY plane normalized to the wavelength; $T(\xi, \eta)$ K is the so-called modified brightness temperature [1].

$$T(\xi,\eta) = \frac{T_B(\xi,\eta)}{\sqrt{1-\xi^2-\eta^2}}\,F_{n1}(\xi,\eta)F_{n2}^*(\xi,\eta) \quad (2)$$

where $T_B(\xi, \eta)$, dimensions of Kelvin, is the brightness temperature; (ξ, η) are the director cosines, with respect the (X, Y) axes, equal $(\sin\theta\cos\phi, \sin\theta\sin\phi)$; $F_{n1,2}(\xi, \eta)$ are the normalized antenna voltage pattern; and $\tilde{r}_{12}(\tau)$, the fringe-wash function, (without units) takes into account spatial decorrelation effects [2].

In the ideal case, no decorrelation effects $\tilde{r}_{12}(\tau) \approx 1$ and identical antenna patterns $F_{n1} = F_{n2} = F_n$, the modified brightness temperature can be recovered by means of a discrete Fourier Transform of the visibility samples

$$T(\xi,\eta) = F^{-1}[V(u,v)]. \quad (3)$$

In large interferometers, in order to simplify the signal distribution network, the cross-correlations are usually performed at baseband by means of real correlators after in-phase and quadrature demodulation

$$V_{1,2} \propto E[i_1(t)i_2(t)] + jE[q_1(t)i_2(t)]. \quad (4)$$

II. Radiometric Sensitivity Computation

Radiometric sensitivity is defined as the minimum input change that can be detected at the output [2]–[4]. In a interferometric radiometer, it is limited by the discretization and the finite coverage of the spatial frequencies plane (u, v) and the SNR, which can be improved by increasing the integration time and/or the predetection bandwidth [3]. The finite (u, v) coverage and the discretization errors set the saturation limit that is reached for high SNR's.

A. Discretization and Finite (u, v) Coverage

In a total-power or Dicke radiometer, the measured antenna temperature is given by equations 4.55–4.60 of [4]. The error committed depends on the particular brightness temperature distribution being observed and can be minimized by maximizing the antenna main-beam efficiency (MBE), which requires the use of antennas with a tapered illumination that, in turn, reduce the achievable spatial resolution.

On the other hand, an interferometric radiometer forms the brightness temperature map by a discrete-inverse Fourier transform of the visibilities measured by the array (3). It has been shown [1], [5], [6] that, as proposed in [7], the optimum shape of a two-dimensional (2-D) interferometric array is a Y. Y-arrays generate the largest regular (u, v) coverage over an hexagonal grid for a given number of antennas, thus maximizing the angular resolution or, conversely, minimizing the hardware requirements [1].

The impulse response of the interferometer in the direction (ξ_0, η_0) can be interpreted as the beam synthesized by the array, and it is called the equivalent array factor $(AF_{\rm eq})$ [3] because of its similarities with phased arrays

$$AF_{\rm eq}(\xi,\eta,\xi_0,\eta_0) = A\sum_n W(u_n,v_n)\tilde{r}_n\left(\frac{u\xi+v\eta}{f_o}\right) \cdot e^{+j2\pi(u(\xi-\xi_0)+v(\eta-\eta_0))} \quad (5)$$

where A is the pixel's area in the (u, v) plane; $A = d^2$ for T-arrays; $A = \sqrt{3}d^2/2$ for Y-arrays; $A = d$ for one-dimensional (1-D) arrays; and d is the spacing between adjacent antennas normalized to the wavelength or the minimum baseline. The function $W(u, v)$ is a window used to weight the visibility samples.

In a similar way, the MBE can be defined as

$$\text{MBE} = \frac{\iint_{\text{main lobe}} |AF_{\rm eq}(\theta,\phi)|\,d\Omega}{\iint_{4\pi} |AF_{\rm eq}(\theta,\phi)|\,d\Omega} \quad (6)$$

where the $AF_{\rm eq}$ is not squared because it refers to brightness temperatures, a power measurement, however, from (5), the $AF_{\rm eq}$ may have negative lobes. The MBE can be optimized by a proper selection of the window function. Table I shows the sidelobe level (SLL) and the MBE at the SLL for five different windows for an Y-array with $N_{\rm EL} = 43$ antennas per arm spaced $d = 0.89$ wavelengths, as proposed for MIRAS [7]. Decorrelation effects have been neglected since $B/f_0 \approx 2\%$. The saturation of the radiometric sensitivity shown in Fig. 1 is due to the discretization or MBE error computed at the center of the instantaneous field of view (FOV) [1]. The error decreases with the array size and the window smoothness.

B. SNR

If the real and imaginary parts of the visibility function are obtained by cross-correlating the in-phase and quadrature components of the signals collected by the antennas once digitalized [7], slightly different results are obtained from those presented in [2], [3], and [8] for the 1-D interferometer ESTAR, or radioastronomy. Three effects that now have been taken into account are predetection filters' shape (rectangular or Gaussian), single sideband (SSB) or double sideband (DSB) receivers with the same predetection bandwidth, and correlator's type.

The MIRAS fringe-wash function was computed in [5] and [6], taking into account the overall frequency response of the receiving chain [7]. It was found that the fringe-wash function is better approximated by a Gaussian filter (7a) than by a rectangular filter (7b) with the same noise bandwidth B (7c).

$$|H(f)| = e^{-\frac{\pi}{2}((f-f_o)/B)^2} \quad (7a)$$

$$|H(f)| = \Pi\left(\frac{f-f_o}{B}\right) \quad (7b)$$

$$B \triangleq \int_{-\infty}^{+\infty} |H(f)|^2\,df \quad (7c)$$

where $\Pi(x) = 1$ for $|x| \le 1/2$ and 0 elsewhere. Consequently, it is expected that more accurate results are obtained with the Gaussian model.

Following the procedure used in [3], the standard deviation of the real and imaginary parts of the visibility function can be computed, taking into account that I/Q demodulation is performed prior to the correlation [6, App. 1]. The main results are listed below for Gaussian (8a) and for rectangular predetection filters (8b)

$$\sigma_{r,i}^2 = \frac{1}{2\sqrt{2}B\tau_{\rm eff}}\Big\{(T_A+T_R)^2\Big[1+e^{-\pi(2\Delta f/\sqrt{2}B)^2}\Big] + V_{r,i}^2(u,v)\Big[1+e^{-\pi(2\Delta f/\sqrt{2}B)^2}\Big] - V_{i,r}^2(u,v)\Big[1-e^{-\pi(2\Delta f/\sqrt{2}B)^2}\Big]\Big\} \quad (8a)$$

TABLE I
SLL [dB] AND MBE FOR THE MIRAS SPACEBORNE-INSTRUMENT EQUIVALENT-ARRAY FACTOR ($\rho_{mn}^2 = u_{mn}^2 + v_{mn}^2$, $\rho_{\max} = \sqrt{3}N_{\mathrm{EL}}d$)

Window	SLL [dB]	MBE (%)
Rectangular $W(u_{mn}, v_{mn}) = 1$	8.4	42.3
Triangular $W(u_{mn}, v_{mn}) = 1 - \frac{\rho_{mn}}{\rho_{\max}}$	11.3	69.3
Hamming $W(u_{mn}, v_{mn}) = 0.54 + 0.46\cos\left(\pi \frac{\rho_{mn}}{\rho_{\max}}\right)$	12.9	78.7
Hanning $W(u_{mn}, v_{mn}) = \frac{1}{2} + \frac{1}{2}\cos\left(\pi \frac{\rho_{mn}}{\rho_{\max}}\right)$	13.8	74.5
Blackmann $W(u_{mn}, v_{mn}) = 0.42 + 0.5\cos\left(\pi \frac{\rho_{mn}}{\rho_{\max}}\right) + 0.08\cos\left(2\pi \frac{\rho_{mn}}{\rho_{\max}}\right)$	16.2	89.6

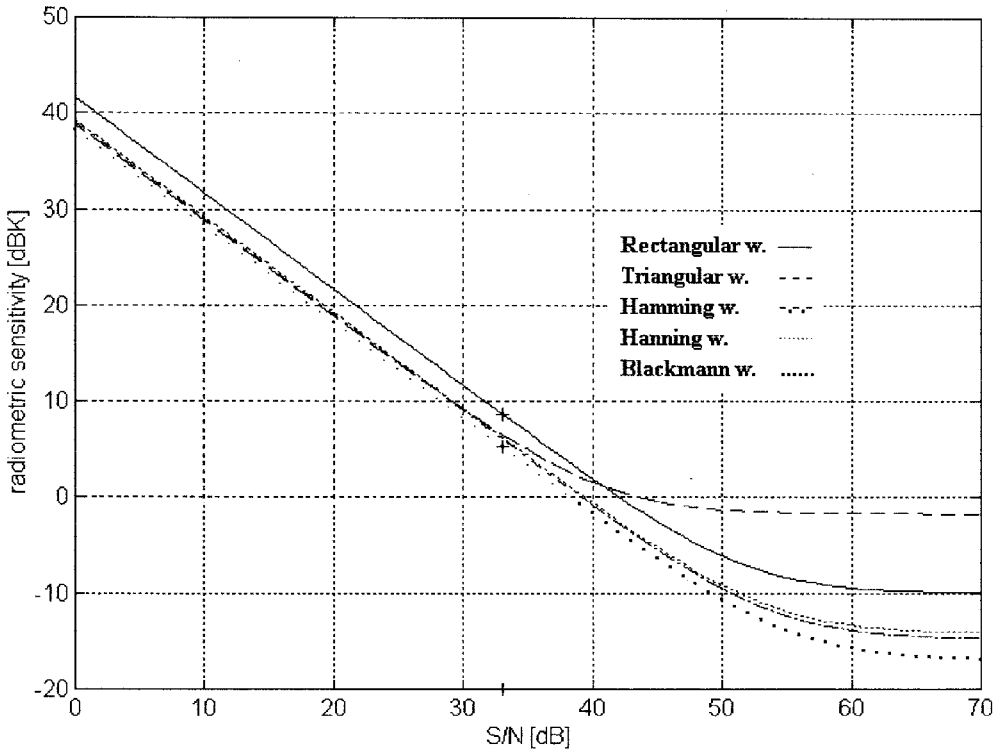

Fig. 1. Radiometric sensitivity dBK (10 log ΔT) versus SNR [10 log (T_A/σ_V)]. T_A = 200 K, MIRAS instrument. Radiometric sensitivity saturation is due to the discretization and finite (u, v) coverage errors.

$$\sigma_{r,i}^2 = \frac{1}{2B\tau_{\mathrm{eff}}}\left\{(T_A + T_R)^2\left[1 + \Lambda\left(\frac{2\Delta f}{B}\right)\right] + V_{r,i}^2(u, v)\left[1 + \Lambda\left(\frac{2\Delta f}{B}\right)\right] - V_{i,r}^2(u, v)\left[1 - \Lambda\left(\frac{2\Delta f}{B}\right)\right]\right\} \quad (8b)$$

where $\Lambda(x) = 1 - |x|$ for $|x| \leq 1$ and 0 elsewhere; V_r and V_i are the real and imaginary parts of the visibility function; T_A is the antenna temperature; $T_R = T_{R1} = T_{R2}$ is the receivers' noise temperature; $\Delta f = f_o - f_{\mathrm{lo}}$ is the difference between the filter's central frequency f_o and the local oscillator's frequency f_{lo}; and τ_{eff} is the effective integration time that depends on correlator's type, i.e., $\tau_{\mathrm{eff}} = \tau$ for an analog correlator, and $\tau_{\mathrm{eff}} = \tau/2.46$ for 1-bit × 1-bit correlator with

sampling frequencies $f_s = 2B$ [9]. At this point, it is interesting to note the following.

1) The variance $\sigma_V^2 = \sigma_r^2 + \sigma_i^2$, computed with rectangular predetection filters, is $\sqrt{2}$ times larger than with Gaussian filters because noise is more compacted in frequency and suffers less from decorrelation effects.
2) For any kind of filter, an improvement by a factor of two is achieved in SSB receivers ($|\Delta f| > B/2$), as compared to DSB receivers ($\Delta f = 0$), at the expense of higher speed correlators and higher power consumption. In practice, the use of SSB demodulation simplifies receiver's design when reradiation from local oscillator to the antenna must be kept below the threshold of the signals received in the protected band, i.e., 1.400–1.427 MHz [7]. It also reduces local oscillator AM noise and offsets can be easily removed by high-pass filtering the signals prior to correlation.
3) The use of digital correlators reduces the integration time τ by a factor that depends on quantization levels and sampling frequency [9].

Since the brightness temperature map is obtained by means of a discrete Fourier transform of the visibility samples, the visibility errors are translated into the temperature map

$$\begin{aligned}\hat{T}(\xi, \eta) = A \sum_m \sum_n W_{mn} \\ \cdot [V(u_{mn}, v_{mn}) + e_{V_r}(u_{mn}, v_{mn}) \\ + j e_{V_i}(u_{mn}, v_{mn})] \\ \cdot e^{j2\pi(u_{mn}\xi + v_{mn}\eta)}\end{aligned} \tag{9}$$

where (e_{Vr}, e_{Vi}) are the errors in the real and imaginary parts of the visibility function. Prior to computation of the radiometric sensitivity some considerations about redundancy and hermiticity must be pointed out.

1) Hermiticity of the Visibility Samples: Only half of the baselines must be measured ($u \geq 0$, $v \geq 0$ and $u < 0$, $v > 0$). The other half is obtained by conjugating the measured baselines. In doing so, the noise is Hermitian too.

$$\begin{aligned}V^*(u, v) &= \left\{\tfrac{1}{2} E[S_1(t) S_2^*(t)]\right\}^* \\ &= \tfrac{1}{2} E[S_2(t) S_1^*(t)] = V(-u, -v).\end{aligned} \tag{10}$$

2) Redundancy and Correlation Between Errors: In [5], [6], [10] and [11], it is shown that the cross-correlation of the errors of two identical baselines 1–2 and 3–4 (except for the antenna positions) with the same integration time τ, one of them delayed τ_d, is given by (rectangular predetection filters)

$$\begin{aligned}E[\Delta V_{12}(t + \tau_d) \Delta V_{34}^*(t)] &= R_{\hat{V}_{12}\hat{V}_{34}}(\tau_d) - V_{12} V_{34}^* \\ &= \frac{V_{13} V_{24}^*}{B\tau_{\text{eff}}} \operatorname{sinc}\left(\frac{\tau_d}{\tau}\right).\end{aligned} \tag{11}$$

being $R_{\hat{V}_{12}\hat{V}_{34}}(\tau_d)$, the cross-correlation between the measured visibilities $\hat{V}_{12}$ and $\hat{V}_{34}$ at $t = \tau_d$. Note that, in an actual onboard interferometer like MIRAS [7], all baselines are measured in the same time interval and $\tau_d = 0$. Given its importance, we explicitly show that the noise of a visibility sample (8b) can be obtained from (11).

$$\begin{aligned}\sigma_V^2 = \sigma_{V_r}^2 + \sigma_{V_i}^2 = E[|\Delta V_{12}|^2] = R_{\Delta V_{12}\Delta V_{12}}(0) \\ = \frac{V_{11} V_{22}^*}{B\tau_{\text{eff}}} = \frac{|V(0, 0)|^2}{B\tau_{\text{eff}}} = \frac{(T_A + T_R)^2}{B\tau_{\text{eff}}}\end{aligned} \tag{12}$$

From (11), it can be seen that, with ideal noise-free receivers, errors between simultaneous measurements ($\tau_d = 0$) of different visibility samples are strongly correlated if the spacing between the antenna pairs 1–2 and 3–4 is much smaller than the downfall of the amplitude of the visibility function. This situation holds for scenes consisting on point sources [2], [10], and averaging simultaneous measurements does not improve SNR significantly. On the contrary, for a smooth temperature distribution, as in the case of earth observation, the visibility function decays rapidly, errors are only partially correlated, and averaging reduces noise power.

On the other hand, if the receiver's noise temperature is much higher than the brightness temperature to be measured, the averaging of simultaneous measurements improves the SNR, due to the reduction of receiver's noise. This is not the case with earth observation at low microwave frequencies, in which receiver's noise temperature ($T_R \approx 80$ K) is usually lower than the average brightness temperature ($T_A \approx 250$ K). In any case, the improvement shown by (13), reproduced from [3], will always be lower than the upper bound found for a linear array, which takes into account uncorrelated errors

$$\begin{aligned}\Delta T_{\text{no redundancy}} &= \frac{T_B + T_R}{\sqrt{B\tau}} \sqrt{N_V} \\ \rightarrow \Delta T_{\substack{\text{redundancy} \\ \text{uncorr errors}}} &= \frac{T_B + T_R}{\sqrt{B\tau}} \sqrt{c + \ln N_V}\end{aligned} \tag{13}$$

where N_V stands for the total number of visibilities and c is the Euler's constant.

A detailed analysis of redundancy and its improvement on radiometric sensitivity requires a specific array configuration and scene under observation. However, for Y-arrays, which provide a very low degree of redundancy [5], [7], [10], [11], this improvement can be approximately found if we realize that only baselines relating antennas on the same arm can be redundant. By the zero baseline it is understood that the one corresponding to $u = v = 0$, which in MIRAS is nonredundant, since it is measured by a dedicated Dicke radiometer. Recall also that when the Hermitian property is considered every (u, v)-point is actually duplicated. For the Y-array with three arms, each with $N_{\text{EL}} = 43$ elements, plus a central element, there are $3N_{\text{EL}}(3N_{\text{EL}} + 1)/2 + 1 = 8386$ baselines [the extra one corresponding to $V(0, 0)$], $3N_{\text{EL}}^2 + 3N_{\text{EL}} + 1 = 5551$ nonredundant baselines or nonredundant (u, v) points, and $3(N_{\text{EL}} - 1) = 126$ redundant (u, v) points with different degrees of redundancy. It means that $8386 - 5551 = 2709$ redundant complex correlations (visibilities) lead to only 126 redundant (u, v) points. This leads to an improvement of a 1% for a 43 antennas per arm Y-array [10], [11], even in the case in which errors between these visibility samples are assumed to be completely uncorrelated.

3) Snapshot Radiometric Sensitivity: As shown in the previous section, visibility errors are Hermitian and, for computational purposes, uncorrelated from sample to sample. With these considerations, the snapshot radiometric sensitivity, that is, the average error in each brightness temperature map obtained after an integration time of τ seconds, is

$$\begin{aligned}\delta T(\xi, \eta) = A \sum_m \sum_n W_{mn} \\ \cdot [e_{V_r}(u_{mn}, v_{mn}) + j e_{V_i}(u_{mn}, v_{mn})] \\ \cdot e^{j2\pi(u_{mn}\xi + v_{mn}\eta\eta)}\end{aligned}$$

$$\begin{aligned}\Delta T(\xi, \eta) &= E[\delta T(\xi, \eta) \delta T(\xi, \eta)^*] \\ &= A^2 \left\{ \sum_m \sum_n W_{mn}^2 (\sigma_{rmn}^2 + \sigma_{imn}^2) \right. \\ &\quad + \sum_{\substack{u_m > 0, v_n \geq 0 \\ u_m \leq 0, v_n > 0}} \sum \sum W_{mn}^2 (\sigma_{rmn}^2 + \sigma_{imn}^2) \\ &\quad \left. \cdot \cos[4\pi(u_{mn}\xi + v_{mn}\eta)] \right\}\end{aligned} \tag{14}$$

TABLE II
BASIC PARAMETERS OF MIRAS INSTRUMENT

Parameter	
Number of antennas per arm	N_{EL} = 43 (11.353 non-redundant visibilities)
Antenna spacing	d = 0.89 wavelengths
Bandwidth	B = 20 MHz
Pre-detection filters' central frequency	f_o = 1.410 MHz
Local oscillator frequency	f_{lo} = 1.395 MHz
Snap-shot integration time	τ = 0.3 seconds
Effective integration time	τ_{eff} = 0.122 seconds
(1 bit x 1 bit digital correlators)	
Receivers' noise temperature	T_R = 80 K
Antenna temperature	100 K $\leq T_A \leq$ 300 K

which can be approximated by

$$\Delta T(\xi, \eta) \simeq A \frac{T_A + T_R}{\sqrt{B\tau_{\text{eff}}}} \alpha_w \frac{\alpha_{ol}}{\alpha_f} \sqrt{N_V} \tag{15}$$

where $A = \sqrt{3}d^2/2$, the local oscillator factor is given by $\alpha_{ol} = \sqrt{2} = 1.41$ for DSB receivers and $\alpha_{ol} = 1$ for SSB receivers; the filter factor is given $\alpha_f = \sqrt[4]{2} = 1.19$ for Gaussian filters and $\alpha_f = 1$ for rectangular filters; and the windowing factor α_w is defined as

$$\alpha_w = \sqrt{\sum_m \sum_n W_{mn}^2 / N_V} \tag{16}$$

where the number of visibility samples, including the Hermitian ones, is $N_V = 6N_{\text{EL}}^2 + 6N_{\text{EL}} + 1$ for Y-arrays. In the MIRAS case, $N_{\text{EL}} = 43$ and the windowing factor $\alpha_w = 1, 0.5212, 0.5717, 0.5446,$ and 0.4517 for the rectangular, triangular, Hamming, Hanning, and Blackmann windows, respectively (Table I). Note that the weighing function attenuates visibility samples between distant antennas, where SNR is worse; thus, the radiometric sensitivity is improved at the expense of a loss in the angular resolution. MIRAS spaceborne snapshot radiometric sensitivity can be computed from (15) and (16) with the parameters listed in Table II [7]. Fig. 1 shows the snapshot radiometric sensibility in decibels $\{10 \log (\Delta T)$ [dBK]$\}$ versus the SNR. For an SNR in the MIRAS range 31.6–33.2 dB, the radiometric sensitivity is bounded by 7.1–15.0 K and 3.2–6.8 K for the rectangular and Blackmann windows, respectively.

4) Radiometric Sensitivity Improvement by Pixel Averaging: Radiometric sensitivity can be improved in a 2-D interferometric radiometer by means of "pixel averaging." That is, since a pixel remains in the FOV for a long time, the recovered values can be averaged after proper correction of the dependence with the angle of incidence. In the MIRAS case, a pixel remains in the FOV for about 22 s (τ_{FOV} = FOV width/platform velocity = 165 Km/7 Km/s = 22 s), from which 11 s correspond to each polarization. The improvement on the radiometric sensitivity in each polarization is then $\Delta T_{\text{pixel avg.}}/\Delta T_{\text{snap-shot}} = \sqrt{(11s/0.3s)} = 6$ or $6\sqrt{2}$ in a single polarization instrument. This improvement is achieved because unsimultaneous measurements are independent and the error is reduced by the square root of the number of measurements, or equivalently, the integration time is increased to the total time the pixel remains in the FOV τ_{FOV}. After pixel averaging, for the MIRAS instrument (dual polarization instrument), the expected radiometric sensitivity values are then $\Delta T^{\text{MIRAS}} \approx 2.5$ and 1.1 K for the rectangular and Blackmann windows, respectively, and $T_A \approx 200$ K.

III. RADIOMETRIC SENSITIVITY IN INTERFEROMETRIC RADIOMETERS AND TOTAL POWER RADIOMETERS: THE INTERFEROMETRIC RADIOMETER UNCERTAINTY PRINCIPLE

In order to compare in a homogeneous way the radiometric sensitivities of interferometric radiometers and ideal total-power radiometers, we must take into account all the available integration time. Note that a 2-D interferometric radiometer images all the space simultaneously, while a total-power radiometer images only the pixel pointed by the antenna beam. That is, the MIRAS spaceborne instrument will image $(3N_{\text{EL}} + 1)^2 = 130^2 = 16.900$ pixels simultaneously [1] every $\tau = 0.3$ s, from which there are 8.689 in the alias-free FOV. An ideal total-power radiometer imaging only the alias-free FOV pixels with the same angular resolution would have a maximum integration time of $\tau_{\text{pixel}} = \tau/8.689 = 0.3\text{s}/8.689 = 34.5$ μs, leading to a worst-case radiometric sensitivity of $\Delta T_{\text{pixel}}^{\text{TPRad}} = T_{\text{sys}}/\sqrt{(B\tau_{\text{pixel}})} \approx 14.5$ K, which is very close to the snapshot radiometric sensitivity of the interferometer radiometer when the rectangular window is used (Section II-B3).

The radiometric sensitivity improvement achieved by windowing can be now understood as the spatial averaging of the pixel's value with its neighbors. In fact, the sensitivity improvement by windowing is approximately related to the half-power synthesized beamwidths given in [6] and [12] by

$$\frac{\Delta T_{\text{rectangular}}^{\text{IntRad}}}{\Delta T_W^{\text{IntRad}}} = \frac{1}{\alpha_W} \simeq \frac{\Delta \xi_W^{-3\text{ dB}}}{\Delta \xi_{\text{rectangular}}^{-3\text{ dB}}}. \tag{17}$$

In [6] and [12], the angular resolution of Y-arrays is analyzed, and for the rectangular window $\Delta\xi_{\text{rect.}}^{-3\text{ dB}} \approx \pi/(4\sqrt{3}N_{\text{EL}}d)$. For an arbitrary window W, the product $\Delta T_W \Delta\xi_{-3\text{dB},W}$ is found to be

$$\begin{aligned}\Delta T_W \Delta\xi^2_{-3\text{ dB},W} &\simeq \frac{\sqrt{3}}{2}\, d^2\, \frac{T_A+T_R}{\sqrt{B\tau_{\text{eff}}}}\, \alpha_w\, \frac{\alpha_{ol}}{\alpha_F}\sqrt{N_V}\, \frac{\pi}{\alpha_w\ 4\sqrt{3}N_{\text{EL}}d} \\ &\simeq \frac{\sqrt{3}\,\pi}{2\ \ 4}\, \frac{T_A+T_R}{\sqrt{B\tau_{\text{eff}}}}\, \frac{\alpha_{ol}}{\alpha_F}, \qquad (N_{\text{EL}}>1) \end{aligned} \tag{18}$$

which can be approximated by

$$\Delta T\ \Delta\xi^2_{-3\text{ dB},W} \simeq \frac{T_A+T_R}{\sqrt{B\tau_{\text{eff}}}}\, \frac{\alpha_{ol}}{\alpha_F} d. \tag{19}$$

Equation (19) is the new Interferometric Radiometer Uncertainty Principle. It states that the product of the radiometric sensitivity ΔT by the 2-D angular resolution $\Delta\xi^2_{-3\text{ dB}}$ is a constant that depends only on receivers and correlators parameters, and it is independent on the window used to process the visibility samples. It can be viewed as the interferometric radiometer version of the total-power radiometer uncertainty equation given in (6.149) of [4].

IV. Conclusions

The radiometric sensitivity of a general 2-D interferometric radiometer has been computed in this paper. The impact of the filters' shape has been analyzed and quantified as well as the type of demodulation (SSB or DSB) and the kind of correlator. The improvement achieved by means of pixel averaging has been discussed and results have been particularized for the MIRAS instrument, a Y-shaped interferometric radiometer with 43 antennas per arm, currently under study at the European Space Agency. It has been shown that after pixel averaging, radiometric sensitivities are expected to be about 2.5 or 1.1 K, depending on the weighing function used to taper the visibility samples. Finally, The new interferometric radiometer uncertainty principle has been stated: it establishes that the product of the radiometric sensitivity by the angular resolution is a constant that depends only on the kind of receivers, correlators, and minimum baselines.

References

[1] A. Camps, J. Bará, I. Corbella, and F. Torres, "The processing of hexagonally sampled signals with standard rectangular techniques: Application to aperture synthesis interferometer radiometers," *IEEE Trans. Geosci. Remote Sensing,* vol. 35, pp. 183–190, Jan. 1997.

[2] R. Thompson, J. Moran, and G. Swenson, *Interferometry and Synthesis in Radio Astronomy.* New York: Wiley, 1986.

[3] C. S. Ruf, C. T. Swift, A. B. Tanner, and D. M. LeVine, "Interferometric synthetic aperture radiometry for the remote sensing of the Earth," *IEEE Trans. Geosci. Remote Sensing,* vol. 26, pp. 597–611, Sept. 1988.

[4] F. T. Ulaby, R. K. Moore, and A. K. Fung, *Microwave Remote Sensing,* vol. I. Norwood, MA: Artech House, 1981.

[5] J. Bará, I. Corbella, F. Torres, and A. Camps, "Two-dimensional discrete formulation for aperture synthesis radiometers," ESA-ESTEC, Final Rep., CNN 2 to Work Order 10 to ESTEC Contract 9777/92/NL/PB, Jan. 1996.

[6] A. Camps, "Application of interferometric radiometry to Earth observation," Ph.D. dissertation, Universitat Politècnica de Catalunya, Barcelona, Spain, Nov. 1996.

[7] Matra Marconi Space, "MIRAS: Microwave imaging radiometer with aperture synthesis. Microwave radiometry critical technical development," ESA-ESTEC, Final Rep., ESTEC Contract 9777/92/NL/PB, Jan. 1995.

[8] M. E. Tiuri, "Radio astronomy receivers," *IEEE Trans. Antennas Propagat.,* vol. AP-11, pp. 930–938, Dec. 1964.

[9] J. B. Hagen and D. T. Farley, "Digital correlation techniques in radio science," *Radio Sci.* vol. 8, pp. 775–784, Aug./Sept. 1973.

[10] J. Bará, A. Camps, F. Torres, and I. Corbella, "Baseline redundancy and radiometric sensitivity: A critical review," in *Soil Moisture and Ocean Salinity Measurements and Radiometer Techniques Consultative Meeting.* Noordwijk, The Netherlands: ESA-ESTEC, Apr. 20–22, 1995.

[11] ——, "The correlation of visibility errors and its impact on the radiometric resolution of an aperture synthesis radiometer," submitted for publication.

[12] ——, "Angular resolution of two-dimensional hexagonally sampled interferometric radiometers," *Radio Sci.,* to be published.

Reciprocity of the Bidirectional Reflectance Distribution Function (BRDF) in Measurements and Models of Structured Surfaces

William C. Snyder

***Abstract*—The bidirectional reflectance distribution function (BRDF) is one of the most important surface properties for terrestrial remote sensing, but its definition for structured surfaces is not fully understood. The BRDF of flat surfaces has a straightforward definition and is usually considered to be reciprocal, which means the value is the same when the source and detector angles are switched. Structured surfaces, such as forest canopies and grasslands, require an extension of the definition of BRDF and some additional measurement conditions. In this paper, a definition for the BRDF of structured surfaces is proposed, and it is shown that with this definition, the BRDF is reciprocal. In addition, some of the related geometrical measurement requirements are discussed. It is concluded that reciprocity should apply for both measurements and models of structured surfaces and that field measurements violate reciprocity not because the BRDF itself is nonreciprocal, but because of uncorrected geometric and radiometric factors.**

***Index Terms*—Electromagnetic scattering by rough surfaces, radiative transfer, radiometry, remote sensing.**

I. Introduction

Land-cover bidirectional reflectance is of prime importance in terrestrial remote sensing. In the solar-reflective region of the spectrum, the bidirectional properties are applied to normalize the effects of different sun-sensor geometries to provide consistent surface features for classification and change detection [1]. In the thermal infrared region, the bidirectional characteristics are applied to account for the reflected downwelling irradiance and to compute the angular emissivity [2]. The bidirectional reflectance distribution function (BRDF) characterizes surface bidirectional reflectance for all combinations of incident and reflected zenith and azimuth angles. BRDF is an optical property of a material that does not depend on external factors, such as illumination or atmospheric transmission. In practice, BRDF can be modeled, but cannot be measured or applied directly

Manuscript received February 19, 1997; revised June 4, 1997. This work was performed at the Institute for Computational Earth System Science, University of California, Santa Barbara, and supported by Earth Observing System Program Contract NAS5-31370 of the National Aeronautics and Space Administration.

The author is with GDE Systems Inc., San Diego, CA 92150-9008 USA (e-mail: will@alumni.caltech.edu).

Publisher Item Identifier S 0196-2892(98)00547-6.